P2.10 HAIL DISDROMETER ARRAY FOR LAUNCH SYSTEMS SUPPORT

John E. Lane *
ASRC Aerospace, Kennedy Space Center, FL
David W. Sharp
National Weather Service, Melbourne, FL
Takis C. Kasparis
University of Central Florida, FL
Nolan J. Doesken
Colorado State University, CO

1. INTRODUCTION

Prior to launch, the space shuttle might be described as a very large thermos bottle containing substantial quantities of cryogenic fuels. Because thermal insulation is a critical design requirement, the external wall of the launch vehicle fuel tank is covered with an insulating foam layer. This foam is fragile and can be damaged by very minor impacts, such as that from small- to medium-size hail, which may go unnoticed. In May 1999, hail damage to the top of the External Tank (ET) of STS-96 required a rollback from the launch pad to the Vehicle Assembly Building (VAB) for repair of the insulating foam. Because of the potential for hail damage to the ET while exposed to the weather, a vigilant hail sentry system using impact transducers was developed as a hail damage warning system and to record and quantify hail events.

The Kennedy Space Center (KSC) Hail Monitor System, a joint effort of the NASA and University Affiliated Spaceport Technology Development Contract (USTDC) Physics Labs, was first deployed for operational testing in the fall of 2006. Volunteers from the Community Collaborative Rain, Hail, and Snow Network (CoCoRaHS) in conjunction with Colorado State University were and continue to be active in testing duplicate hail monitor systems at sites in the hail prone high plains of Colorado.

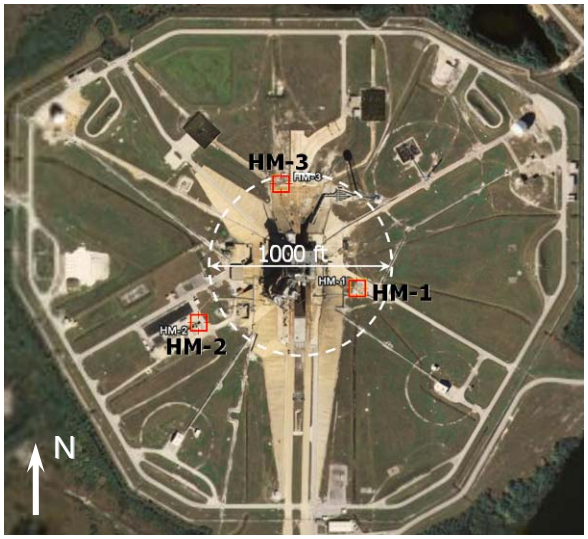

Figure 1. Hail monitor stations at Pad 39A.

The KSC Hail Monitor System (HMS), consisting of three stations positioned approximately 500 ft from the launch pad and forming an approximate equilateral triangle (see Figure 1), was deployed to Pad 39B for support of STS-115. Two months later, the HMS was deployed to Pad 39A for support of STS-116. During support of STS-117 in late February 2007, an unusual hail event occurred in the immediate vicinity of the exposed space shuttle and launch pad. Hail data of this event was collected by the HMS and analyzed.

Support of STS-118 revealed another important application of the hail monitor system. Ground Instrumentation personnel check the hail monitors daily when a vehicle is on the launch pad, with special attention after any storm suspected of containing hail. If no hail is recorded by the HMS, the vehicle and pad inspection team has no need to conduct a thorough inspection of the vehicle immediately following a storm. On the afternoon of July 13, 2007, hail on the ground was reported by observers at the VAB, about three miles west of Pad 39A, as well as at several other locations around Kennedy Space Center. The HMS showed no impact detections, indicating that the shuttle had not been damaged by any of the numerous hail events which occurred that day.

2. HAIL DISDROMETER

Impact disdrometers (Joss, 1967) have long been a useful meteorological tool for measuring rainfall drop size distributions. The electrical impulse generated from a raindrop impact with the sensor head is converted to an estimate of drop diameter by means of an empirical calibration formula. The calibration may be a one-time procedure involving dropping numerous known-size-calibration drops from a tower of sufficient height to achieve terminal velocity. Alternatively, or as a supplement to the single drop calibration, an in situ method of comparing the total integrated volume of disdrometer measured drops per synchronized collocated tipping bucket rain gauge tip, as described by Lane (1997), or in the case of a hail disdrometer, the time integrated histograms

* *Corresponding author address:* John E. Lane, ASRC Aerospace, ASRC-15, Kennedy Space Center, FL, 321-867-6939; e-mail: John.E.Lane@nasa.gov.

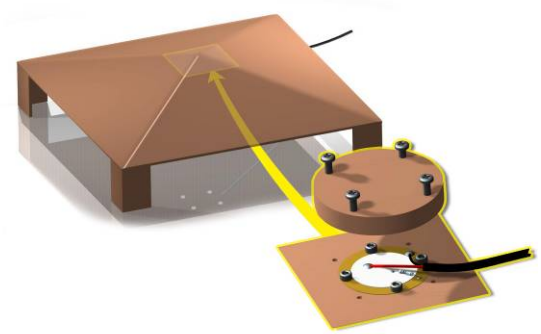

Figure 2. CAD drawing of hail disdrometer impact sensor, showing placement of piezoelectric transducer.

of hail disdrometer spectra to collocated hail pads (Lane, 2006) can be utilized.

The hail disdrometer follows the design principles of the rainfall disdrometer. The hail sensor is composed of four aluminum sheet metal plates welded to the shape of a shallow pyramid. The sloped surface deflects hail, preventing multiple bounces from the same hail stone. A piezoelectric microphone element is mounted beneath and in the center of the pyramid (see Figure 2). The output of this microphone is connected to an electronic circuit which digitizes and processes the electrical signal, and then transmits a trigger pulse to one of six output channels. Each output channel represents a signal that is twice as large as the previous channel, thereby categorizing the hail stone into one of six sizes, from diameters of about 10 mm to 20 mm, in 2 mm steps. The six output channels are connected to six LCD counters, which create a permanent record of all hail hitting the sensor. The counters are manually reset after a hail storm.

Figure 3. Site 3 hail monitor unit at Pad 39A.

3. HYDROMETEOR SIZE DISTRIBUTIONS

The physical connection between rainfall rate measured by ground instruments and rainfall estimated by weather radar is the *drop size distribution* (DSD). If the DSD is somehow previously known as a continuous function of time and space, radar reflectivity Z can be directly calculated from the spatial average of the sixth moment of the DSD. Using hydrometeor terminal velocity values, rainfall rate R can be also be calculated at any point on the ground if the DSD is known at ground level and air motion is assumed to be zero near the ground.

Direct DSD measurements can be made at a point on the ground using a disdrometer. By applying the equations of motion for non-interacting hydrometeors, a spatial and temporal estimate of the DSD in a volume surrounding ground measuring stations can be obtained from a microscale array of disdrometers by employing a horizontal interpolation and vertical extrapolation algorithm such as the 3D-DSD (Lane, 2002a). The sampling volume is characterized by wind velocities, which are input parameters to the 3D-DSD model, composed of vertical (updraft/downdraft) and horizontal (advection) components. The 3D-DSD algorithm assumes that only gravity and terminal velocity due to atmospheric drag within the sampling volume influence hydrometeor dynamics, i.e., hydrometeor interactions are ignored.

3.1 *Gravitational Sorting of Hydrometeors*

Gravitational sorting of hydrometeors is a well known meteorological phenomenon. Disdrometers are well suited to measuring this characteristic of convective storms. However, the standard binning of disdrometer size data can mask the details of gravitational sorting. In order to study gravitational sorting it is necessary to operate a disdrometer in a diameter versus time (D-t) mode, e.g., McFarquhar (1996).

Useful information can be extracted from D-t plots using a crude model of drop dynamics. For simplicity, the hydrometeor terminal velocity can be approximated by a power-law:

$$v_T(D) \approx KD^p \qquad (1)$$

Even though better approximations have been proposed, Equation (1) with p = 1/2 and K = 4.4 [m s^{-1} mm$^{-1/2}$] is a reasonable approximation for both rain and hail.

The fall time of a hydrometeor from some effective starting height h at $t = t_0$ can be expressed by:

$$\tau(D) = \frac{h}{v_T(D) - w} \qquad (2)$$

where w is the vertical component of ambient air motion (positive direction is up). Substituting Equation

(1) into (2) and solving for D results in a predicted gravitational sorting of size diameters at the ground as a function of time:

$$D(t) = \left(\frac{h + w(t - t_0)}{K(t - t_0)} \right)^{1/p} \tag{3}$$

where $\tau = t - t_0$.

Figure 4 shows a D-t scatter plot (Lane, 2002b) from one disdrometer of a three disdrometer array, located approximately 16 km north of the Melbourne NWS radar. This plot of D-t corresponds to a convective storm that occurred on the afternoon of July 19, 2001, beginning at 22:40 UTC. Equation (3) is superimposed with various values of h and w. As can be seen, h and w can not easily be uncoupled, however, the general shape of the curve is significant.

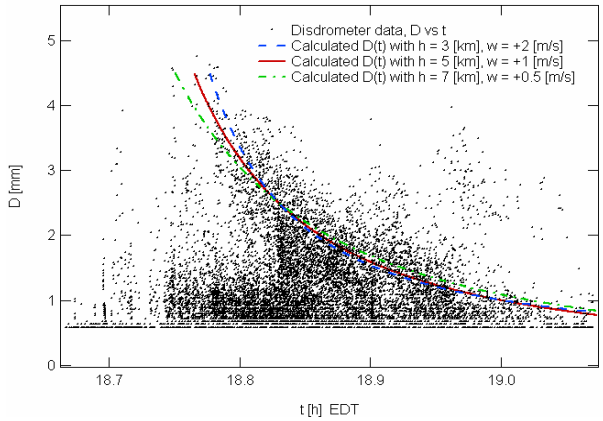

Figure 4. Disdrometer D-t data with calculated D(t) from Equation (3).

The main point of the above discussion is to demonstrate that hydrometeor trajectory analysis can be performed, yielding useable results, based on a crude model that does not consider hydrometeor interactions. This point leads to the 3D-DSD model.

3.2 *3D-DSD Algorithm*

For the jth diameter size bin of width ΔD (valid for either rain or hail), corresponding to a hydrometeor diameter of $D_j \equiv j\Delta D$, the fall time Δt_j of the hydrometeor, based on its terminal velocity $v_T(D_j)$, is:

$$\Delta t_j = \Delta z / v_T(D_j) \tag{4}$$

where Δz is the vertical distance of fall during time interval Δt_j. The corresponding horizontal distances Δx_j and Δy_j, corresponding to the time interval Δt_j, are:

$$\Delta x_j = u_x \, \Delta z / v_T(D_j) \tag{5a}$$

$$\Delta y_j = u_y \, \Delta z / v_T(D_j) \tag{5b}$$

Together, Equations (4) and (5) describe the linear trajectory of a raindrop packet η_j of size D_j, traveling at a constant velocity $\vec{v}_j$, formed by the vector sum of the cloud advection and drop terminal velocities:

$$\vec{v}_j = u_x \, \hat{e}_x + u_y \, \hat{e}_y - v_T(D_j) \, \hat{e}_z \tag{6}$$

where $\hat{e}_x$, $\hat{e}_y$ and $\hat{e}_z$ are unit vectors in the x, y and z directions, while u_x and u_y are the components of the advection velocity. The number of drops per unit volume, described by the jth drop size packet $\eta_j(x, y, z, t)$, is related to the continuous drop size distribution function $N(x, y, z, t; D)$ by:

$$\sum_{j=1}^{M} \eta_j(x, y, z, t) \approx \int_0^{\infty} N(x, y, z, t; D) \, dD \tag{7}$$

Using a microscale disdrometer array, $\eta_j(x, y, z_0, t)$ can be estimated by interpolating the drop count histograms between each disdrometer of the array, where the interpolation is performed over x and y independently (z_0 is the ground level), for each of the jth drop size bins. The disdrometer histogram bins are first divided by the product of the histogram measurement time interval, disdrometer sensing area, and drop terminal velocity, in order to achieve units of m^{-3} (i.e., drops per unit volume). Once $\eta_j(x, y, z_0, t)$ has been estimated from the disdrometer array data, a interpolation to z yields the 3D-DSD model:

$$\eta_j(x, y, z, t) \approx \eta_j(x', y', z_0, t') \tag{8}$$

Using Equations (4) and (5), the primed and unprimed coordinate systems in Equation (8) are related by:

$$\begin{aligned} x' &= x + u_x \, \Delta t_j = x + u_x \, z / v_T(D) \\ y' &= y + u_y \, \Delta t_j = y + u_y \, z / v_T(D) \\ t' &= t + \Delta t_j = t + z / v_T(D) \end{aligned} \tag{9}$$

According to the description established by Equations (8) and (9), a 3D-DSD can be estimated at any x, y, z and t by transforming to a primed coordinate system at z_0 (ground level) where the DSD has been determined by measurement and interpolation.

Reflectivity is calculated as the 6th moment of the 3D-DSD:

$$\begin{aligned} Z(x, y, z, t) &= \sum_{j=1}^{M} D_j^6 \, \eta_j(x, y, z, t) \\ &\approx \sum_{j=1}^{M} D_j^6 \, \eta_j(x', y', z_0, t') \end{aligned} \tag{10}$$

Equation (10) has strong similarities to a *convolution sum* due to the time delay (and spatial offset) caused by the dependence of the primed coordinates on the drop diameter D. The kth disdrometer is located at $\{x_k, y_k, z_0\}$, so that $Z(x_k, y_k, z_0, t)$ from Equation (10) is equivalent to the traditional reflectivity calculated from a point disdrometer. In order to compute a 3D-DSD estimate of disdrometer derived radar reflectivity for comparison to WSR-88D radar reflectivity, it is necessary to average Equation (10) over the appropriate extent of x, y and z.

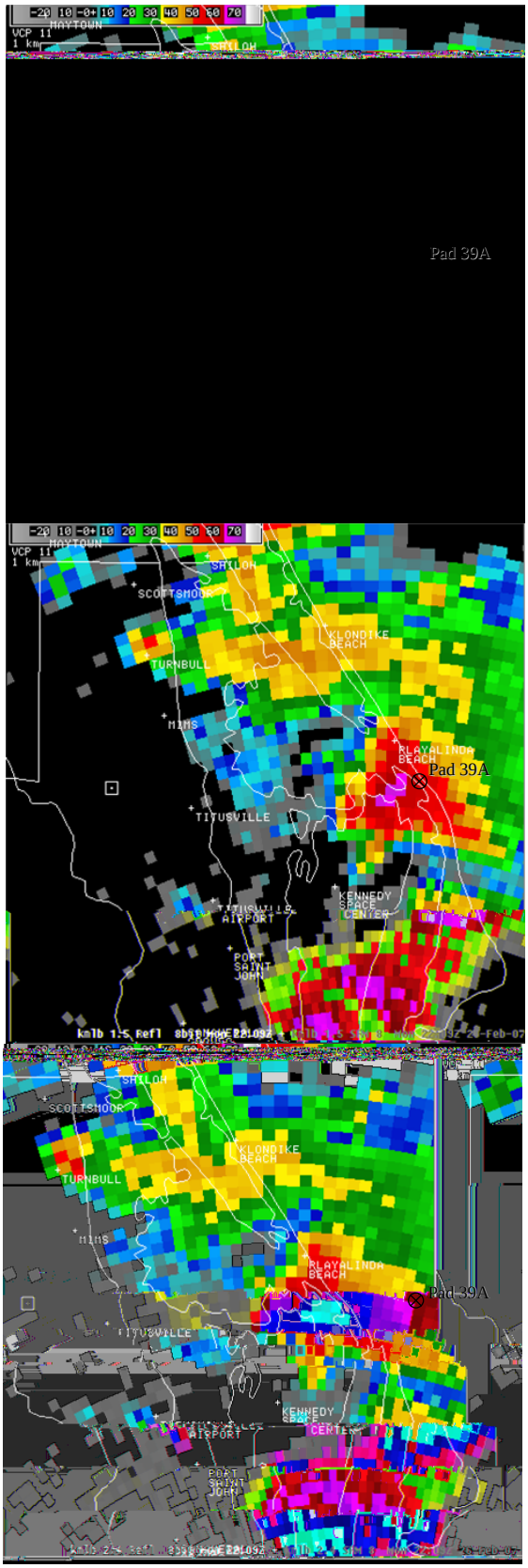

Figure 5a. Melbourne WSR-88D, lowest three reflectivity scan elevations (top to bottom) at 22:09 UTC, Feb 26, 2007.

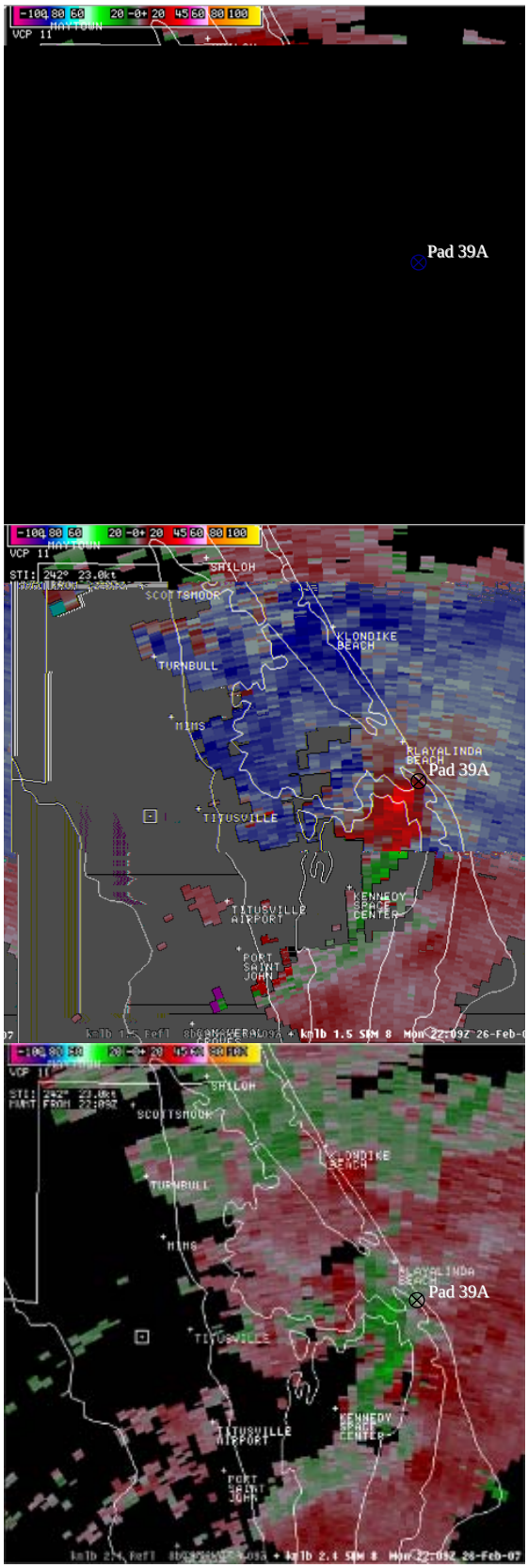

Figure 5b. Melbourne WSR-88D lowest three storm relative radial velocity scans (top to bottom) at 22:09 UTC, Feb 26, 2007.

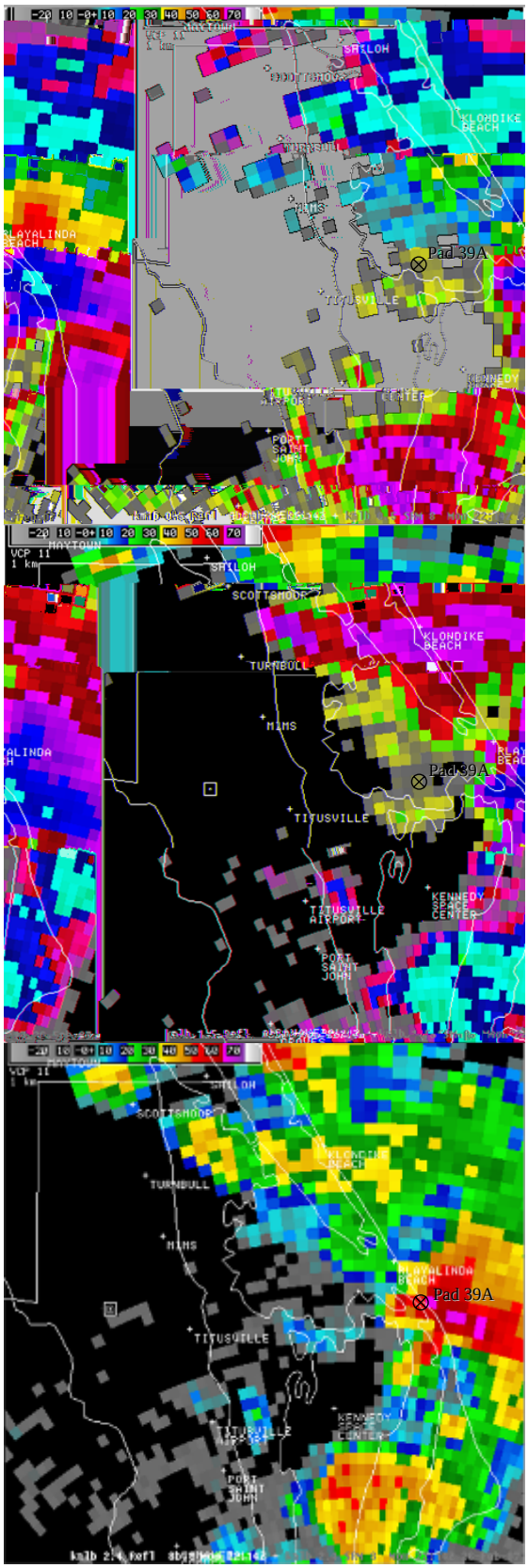

Figure 6a. Melbourne WSR-88D, lowest three reflectivity scan elevations (top to bottom) at 22:14 UTC, Feb 26, 2007.

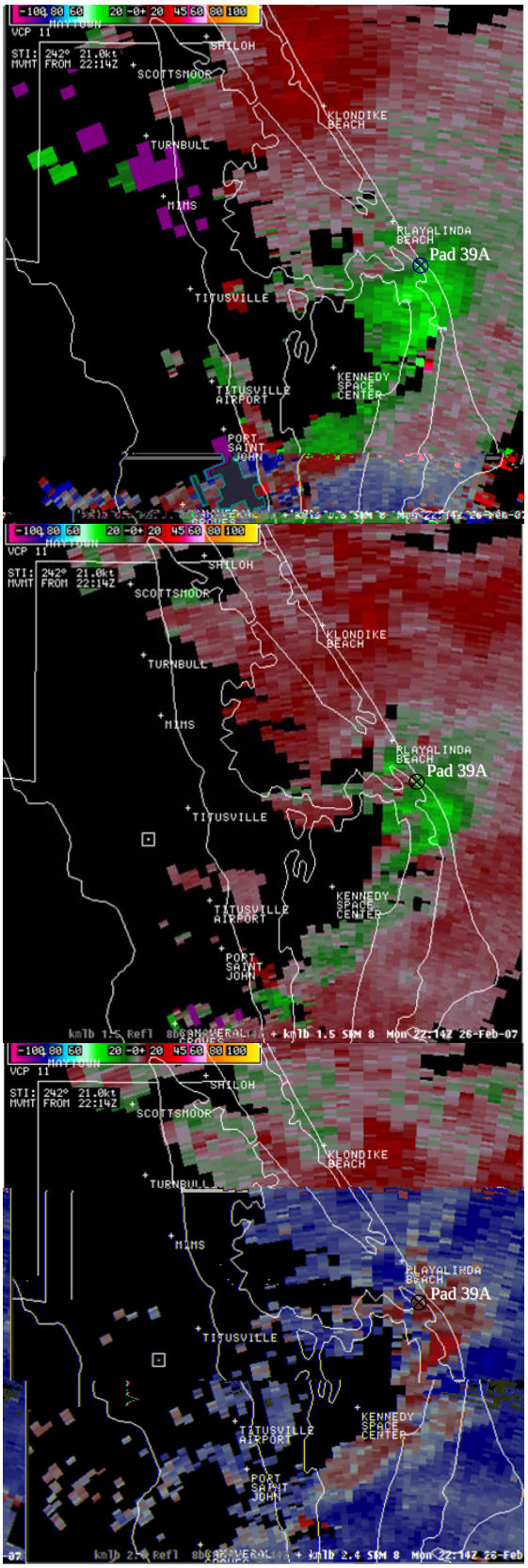

Figure 6b. Melbourne WSR-88D lowest three storm relative radial velocity scans (top to bottom) at 22:14 UTC, Feb 26, 2007.

4. SEVERE HAIL EVENT AT PAD 39A

The prototype hail monitor system (see Figure 3) was in operation at Pad 39A at the time of the February 26, 2007 severe hail event (hail stones ≥ 19 [mm]). On this day the atmosphere over the Florida Peninsula was conditionally poised for scattered deep convection. The 1500 UTC Cape Canaveral sounding analysis (XMR) revealed 500 mb temperatures around -14 C with a mean-layer convective available potential energy calculated near 1500 J/kg. Despite area cloudiness, afternoon surface temperatures were anticipated to near 27 C. A southward sagging cold front was located over northern Florida leaving the KSC situated in the synoptic warm sector with vicinity dew point temperatures of 17 to 19 C. Opportunity for favorable jet dynamics aloft was evident with the right rear quadrant of an upper-level jet forecast to move across the peninsula late in the day along with an increasing low-level jet of 15 m/s (~30 kt) out of the west. Surface winds were southwest at 5 to 8 m/s (~ 10 to 15 kt) with nearly unidirectional flow above, and with increasing speed shear with height. The 0-6 km shear was 25 to 30 m/s (~ 50 to 60 kt). The assessed threat was for isolated severe storms to develop late in the afternoon and move east at 12 to 15 m/s (~25 to 30 kt). The associated main hazards were large hail, straight line winds, and excessive cloud-to-ground lightning. By 21:00 UTC, strong convection had broken out over eastern Orange County and at 21:33 UTC a warning was issued for eastern Orange County and northern Brevard County for an isolated severe thunderstorm moving toward KSC. Transitioning from the rapid growth phase into the mature phase, an apparent "donut" signature was noted on the Lightning Detection and Ranging (LDAR) system. The LDAR system provides 3-D and 4-D total lightning information in proximity of the sensor network located on KSC and is especially useful for storm-cell interrogation when used in conjunction with weather radar. This apparent donut (e.g., lightning-free hole), along with an increased trend in the total signal count, helped discern the extreme intensity of the rotating updraft and bolstered forecaster confidence that the worst was yet to occur. Unfortunately, severe weather manifestation (with respect to large hail, stones ≥ 19 [mm] at the surface) occurred before the storm could move offshore and away from the shuttle launch pad and KSC compound.

4.1 *Melbourne WSR-88D*

Volumetrically, a once elevated core of very high reflectivity (~70 dBZ) rapidly descended to the surface as shown in the lowest elevation slice at 22:09 UTC of Figure 5a. Large hail aloft was no longer being suspended by the intense updraft, signaling a shift to the downdraft dominated phase of this severe local storm. This phase represents the surface impact phase; the dangerous phase in this scenario. The storm-relative velocity (Figure 5b) shows broad cyclonic vorticity surrounding the main core and denoting some descending angular momentum influenced from organized mid-level rotation noted several volume scans earlier (the organized mid-level rotation and storm tilt with height allowed hail embryos to be suspended for longer periods with preferred trajectories for greater growth opportunity). At 22:09 UTC, although radial magnitudes were notably high, the area was broad (not an intense gate-to-gate couplet; not a significant tornado threat). A flanking gust front moving east southeast across the Pad 39A was situated near and to the immediate southwest, with subsequent low-level convergence just ahead of it (promoting additional cellular growth). Relative to Pad 39A, the strongest winds and largest hail appeared to hit between 22:09 UTC and 22:14 UTC (Figures 6a and 6b). Accelerated winds of 25 to 30 m/s (~49 to 58 kt) were noted south of the pad, as well as a turbulent eddy (or possible gustnado/funnel).

4.2 *Hail Pad Data*

Data from the Pad 39A hail monitor system recorded hail diameters up to 20 [mm]. Collocated hail pads (Styrofoam covered with aluminum foil, based on the CoCoRaHS design and fabrication methods) suggest hail sizes up to 35 [mm] may have occurred at Sites-2 and -3 (see Figures 8 and 9). A hail pad calibration method developed during the 1978 Alberta

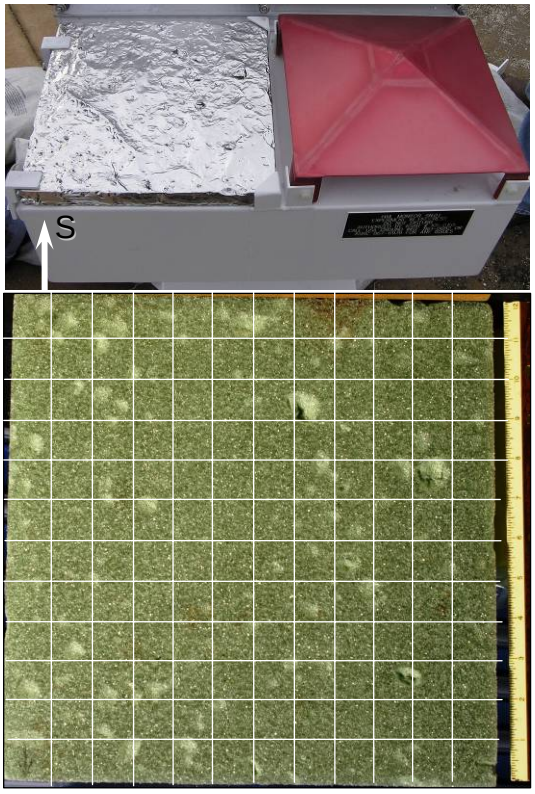

Figure 7. Site-1 hail pad after Feb 26 hail event; (bottom) foil removed, with 1 x 1 [in] grid.

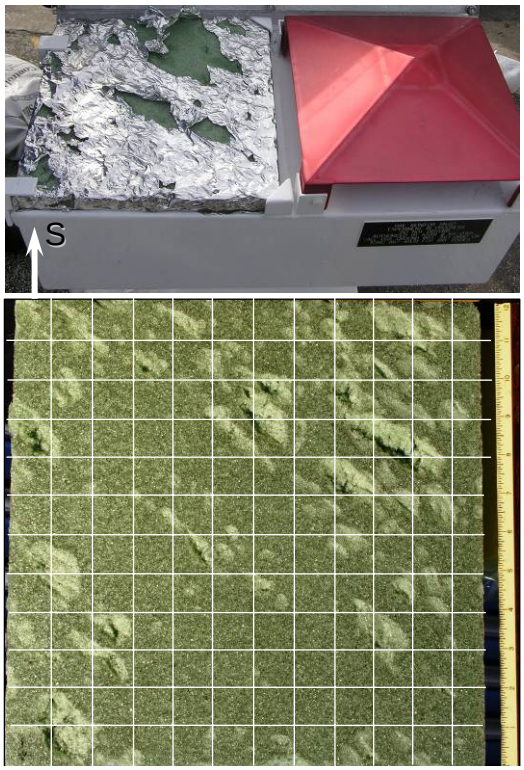

Figure 8. Site-2 hail pad after Feb 26 hail event; (bottom) foil removed, with 1 x 1 [in] grid.

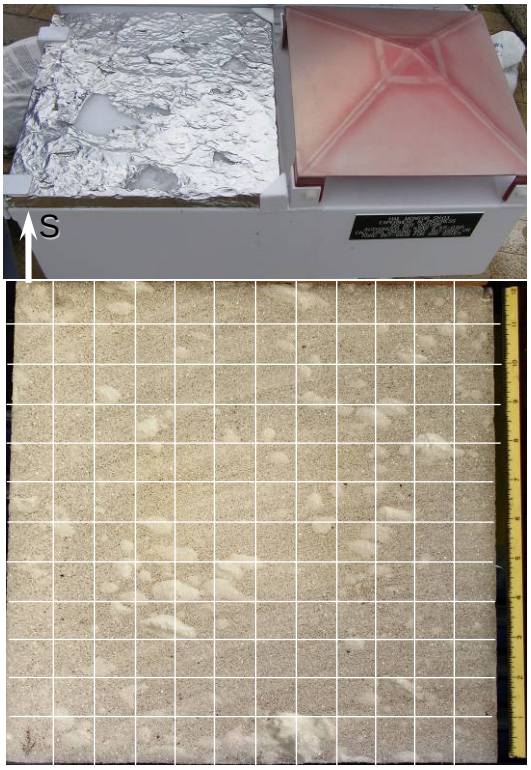

Figure 9. Site-3 hail pad after Feb 26 hail event; (bottom) foil removed, with 1 x 1 [in] grid.

Hail Project relates the dent diameter D to the hail diameter D' as an empirical second-order polynomial (Strong, 1977):

$$D' = a_0 + a_1 D + a_2 D^2 \qquad (11)$$

where a_0 = 0.38 [cm], a_1 = 1.11, and a_2 = −0.04 [cm^{-1}]. Other calibration formulas have since been developed (Lozowski, 1978), as well as calibrations for hail pads made from alternate materials, such as foam rubber covered with aluminum foil (Waldvogel, 1978b), and Styrofoam covered with white latex paint (Long, 1980).

Two of three hail pads at Sites-2 and -3, experienced hail driven by violent horizontal winds thus shredding the foil (see Figures 7 through 9). A small number of hail pads with shredded foil are seen every year by the Colorado State University managed CoCoRaHS network of hail observers, usually only occurring when numerous stones of moderate to large size are driven by strong winds. Out of the many powerful hail storms that occur in Colorado each year, only about one out of every 100 or so hail pads are retrieved with significantly torn foil.

The large impact angle deviation from normal incidence makes the 30-35 [mm] hail pad deduced maximum diameters at Sites-2 and -3, most likely an overestimate due to the gouging effect as opposed to the denting mechanism of a normal incidence impact at terminal velocity. However, the fact that gouging occurred, is relevant to the total kinetic energy and hail damage potential on the shuttle ET foam.

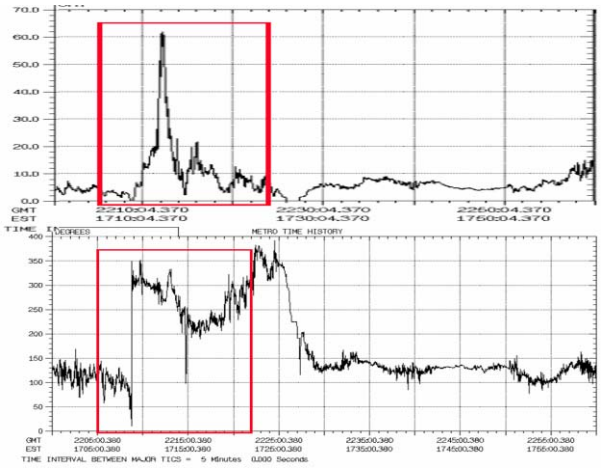

Figure 10. Pad 39A wind tower data showing a 60 [kt] peak from 270°, with a duration of about one minute.

4.3 *Hailstone Spectra*

Rainfall disdrometer data leads directly to an estimation of the corresponding rainfall DSD. Rainfall DSD estimates can then be used to compute an

equivalent radar reflectivity via a discrete evaluation of the 6th moment of the DSD. An estimation of rainfall rate can also be performed via discrete integration (summation of histogram bin products) using raindrop terminal velocity estimates.

Table 1. Hail disdrometer size channel counts.

	HM Site-1		HM Site-2		HM Site-3	
Chan, k	D_k [mm]	Cnt, h_k	D_k [mm]	Cnt, h_k	D_k [mm]	Cnt, h_k
1	10.7	28	11.4	124	9.6	103
2	12.8	45	13.9	39	12.0	89
3	14.5	11	15.9	8	13.9	24
4	16.2	0	17.9	2	15.8	5
5	17.9	0	19.9	0	17.7	1
6	>18.7	0	>20.9	0	>18.6	0

Table 2. Hail disdrometer counts per 60 [s] interval.

	HM Site-1	HM Site-2	HM Site-3
	Logger clock offset correction = 0 [s]	Logger clock offset correction = -24 [s]	Logger clock offset correction = +6 [s]
Time t_j	Tot Cnt, w_j	Tot Cnt, w_j	Tot Cnt, w_j
22:09	0	0	0
22:10	0	0	1
22:11	4	38	96
22:12	57	112	109
22:13	18	10	6
22:14	3	10	7
22:15	1	2	0
22:16	0	1	3
22:17	1	0	0
22:18	0	2	1
22:19	0	0	0

In the case of hailstone spectrometers (see for example Waldvogel, 1978a), a hail impact disdrometer, such as that used in the Pad 39A hail monitor system is a subset of that class of instruments. Hail size distributions (HSD) can also be computed from hailstone spectra, along with an equivalent radar reflectivity (of hail only). Instead of a *hail fall rate* equivalent to rainfall rate, a *hailstone kinetic energy flux* is more often the quantity of interest, since the kinetic energy flux or total integrated energy is more relevant to damage caused by hail, e.g., Visser (2000).

Kinetic energy flux $\dot{E}_H$ [J m^{-2} s^{-1}] is defined by Waldvogel (1978a) as:

$$\dot{E}_H = \frac{\pi\rho}{12\times10^6}\int_0^\infty N_H(D)D^3 v_T^3\, dD \qquad (12)$$

where ρ [gm cm^{-3}] is the density of hail, $N_H(D)$ [m^{-3} mm^{-1}] is the hail size distribution (HSD), and v_T is hail stone terminal velocity, such as that approximated by Equation (1). The total kinetic energy E_H [J m^{-2}] per unit area is just the time integral of Equation (12) over the duration of the hail event.

The kinetic energy associated with the Feb 26 hail event at Pad 39A can be computed from the hail disdrometer data shown in Table 1 and by using a discrete version of the time integral of Equation (12):

$$E_H = \frac{\pi\rho}{12\times10^6}\frac{1}{A_s}\sum_{k=1}^{M} h_k D_k^3 v_{T_k}^3 \qquad (13)$$

where h_k is the kth channel count corresponding to D_k from Table 1, and $v_{Tk} = v_T(D_k)$ from Equation (1). A_s is the disdrometer sensor area, equal to one sq ft or 0.093 [m^2].

The result of evaluating Equation (13) for each of the three hail monitor sites is summarized in Table 3. These values are reasonable when compared to published kinetic energy flux, e.g. Visser (2000), of $\dot{E}_H \approx 1.8$ [J m^{-2} s^{-1}] for radar reflectivity values of 66 dBZ. The energy flux is estimated in Table 3 by dividing the total energy density by Δt = 120 [s], which is the approximate time interval of the majority of the

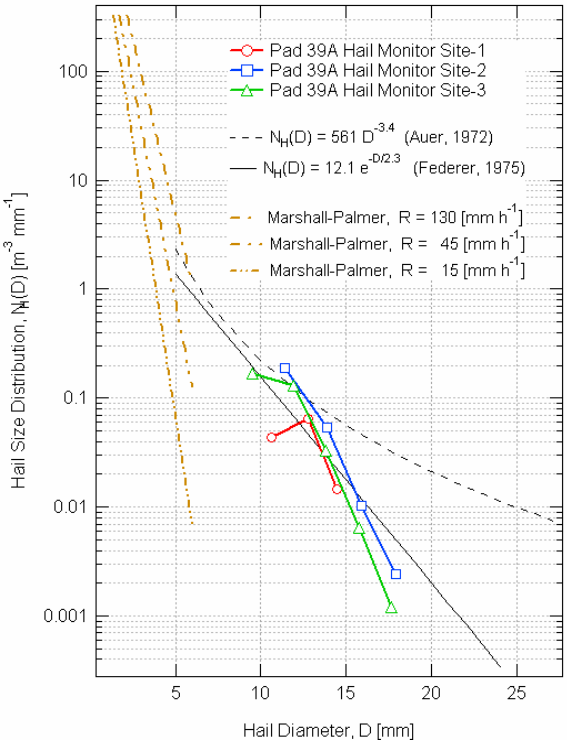

Figure 11. Hail size distribution for the Feb 26, 2007 event calculated using Equation (13) with Pad 39A hail data from Table 1. Note comparison to HSD models from Federer (1975) and from Auer (1972).

hail fall. Since the hail disdrometer at Site-1 was located on the leeward side of the pad and was therefore partially sheltered from the hail event, it is not surprising to see an energy flux value that is smaller than the other two sites.

Table 3. Total kinetic energy and estimated flux of Feb 26 hail event, with Δt = 120 [s].

	HM Site-1	HM Site-2	HM Site-3
E_H [J m^{-2}]	99.6	209.5	194.4
$\dot{E}_H \approx \frac{E_H}{\Delta t}$ [J m^{-2} s^{-1}]	0.83	1.75	1.62

The hail size distribution, $N_H(D)$ [m^{-3} mm^{-1}], can be calculated from the histogram data in Table 1 and the following equation:

$$N_H(D_k) = \frac{h_k}{A_s v_{Tk} \Delta t \, \Delta D} \qquad (13)$$

where h_k is again the kth channel hail impact count corresponding to D_k in Table 1; $v_{Tk} = v_T(D_k)$ from Equation (1); A_s = 0.093 [m^2] ; Δt = 240 [s] (a longer event interval than the energy flux case); and $\Delta D \approx$ 2.0 [mm]. The result is plotted in Figure 11 and for comparison, Marshall-Palmer model plots of rainfall DSDs for various values of rainfall rate, as well as some published hail size distribution (HSD) models.

The HSD plots from Pad 39A in Figure 11 agree reasonably well with Federer (1975). Agreement with Auer (1972) below hail diameters of 15 [mm] is also fair. The droop and cut-off of the Pad 39A HSD below 12 [mm] is most likely due to the calibration of the hail disdrometers and software cut-off limit which was set to aggressively discriminate rain from hail, i.e., adjusted for a low probability of false detection. This threshold may be moved to a lower value with some increased risk of false detections from rain.

4.4 *3D-DSD Plots*

Using the hail disdrometer array data from Tables 1 and 2, as well as Equation (10) as a starting point, a disdrometer derived radar reflectivity can be computed for comparison to the NWS WSR-88D (see Figure 12). Several steps need to be taken in order to optimize this comparison:

- Vertical (updraft/downdraft) and horizontal (advection) wind velocities are used to refine the calculations of Equation (10), as discussed by Lane (2002b).
- The time and location of the corresponding WSR-88D reflectivity bin center is used in Equation (10) for each computation of x, y, z, and t in the disdrometer 3D-DSD plot of equivalent reflectivity.

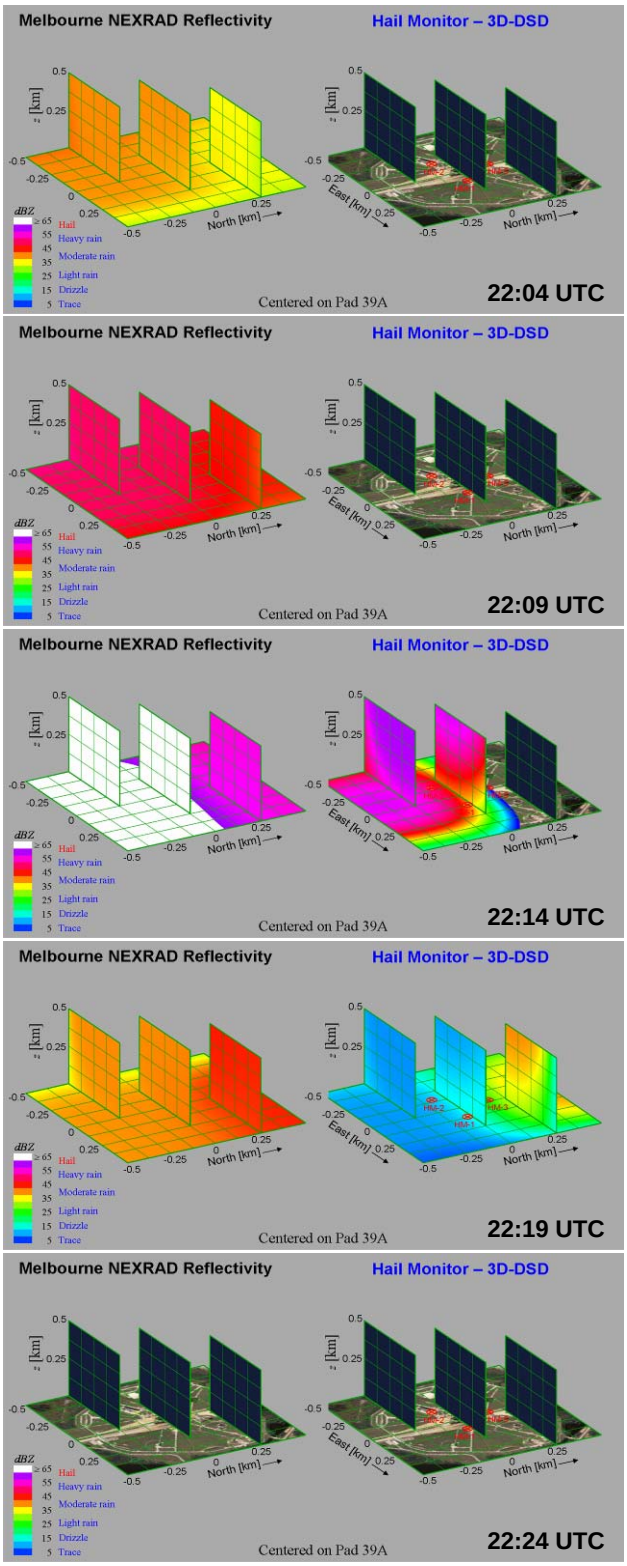

Figure 12. Comparisons of WSR-88D radar reflectivity and equivalent radar reflectivity from 3D-DSD algorithm calculated using Equation (10) and hail disdrometer data from Tables 1 and 2.

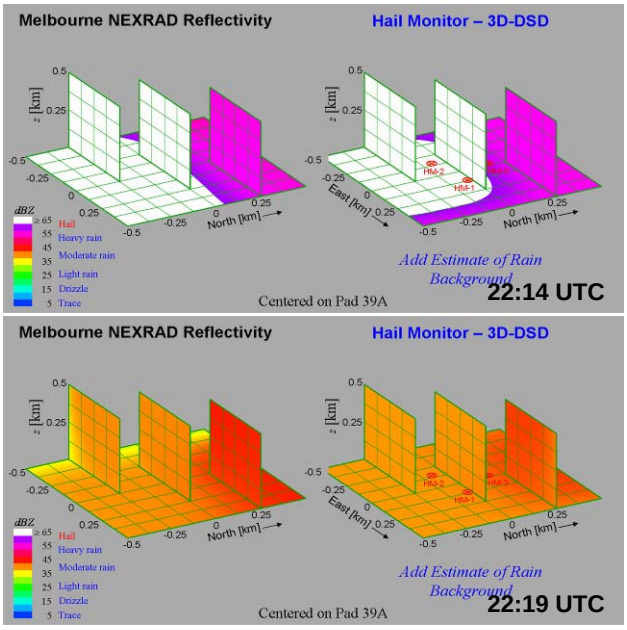

Figure 13. Same comparisons as 3rd and 4th set of Figure 12, but with the addition of a rainfall background based on the Marshall-Palmer drop size distribution; (top) background R = 130 [mm h^{-1}]; (bottom) background R = 10 [mm h^{-1}].

- Equation (10) is computed for numerous adjacent values of x, y, and z, then averaged in order to approximately match radar reflectivity averaged over a radar bin.
- A Marshall-Palmer rainfall DSD background is added to the argument of the summation in Equation (10), as shown in Figure 13.

The plots of Figure 12 and 13 are centered over Pad 39A, and represent a 1 [km] × 1 [km] horizontal extent with a 0.5 [km] vertical extent. Figure 12 shows comparisons of WSR-88D radar reflectivity and equivalent radar reflectivity from the 3D-DSD algorithm of Equation (10), where the plotted disdrometer derived radar reflectivity is due to the contribution from hail only.

Figure 13 shows the same comparisons as the 22:14 UTC and 22:19 UTC scans of Figure 12, but with the addition of a rainfall background based on the Marshall-Palmer drop size distribution. The 22:14 UTC scan uses a background R = 130 [mm h^{-1}]. The 22:19 UTC scan uses a background R = 10 [mm h^{-1}].

5. CONCLUSIONS

The hail swath that damaged STS-117 on Pad 39A, just brushed the pad structures. This was very fortunate, since the main core of the hail was roughly 1 [km] or so to the south. According to data analysis, the worst part of the hail swath which contained the larger hail, ended just beyond the pad structures, and was composed of only small hail stones at the north perimeter fence line, about 0.5 [km] from the pad center. The unfortunate part was that the hail was driven by a 60 [kt] horizontal wind for roughly 1 [min]. Those conditions undoubtedly led to the hail damage on the vehicle's ET. Based on radar and hail disdrometer data, it is clear that the hail at pad 39A was embedded in intense rainfall of a high rainfall rate.

The HMS consisting of three hail disdrometers, has proven to be a useful hail monitoring and post analysis tool for shuttle launch pad ground support. The 3D-DSD algorithm, coupled with other instrument data, such as Kennedy Space Center wind tower and Melbourne NWS radar, provide a high resolution picture of hail events on a spatial resolution of meters, and a temporal scale of seconds.

6. REFERENCES

Auer, A.H., Jr., 1972: Distribution of graupel and hail with size. *Mon. Wea. Rev.*, **100**, 325-328.

Federer, B., and A. Waldvogel, 1975: Hail and Raindrop Size Distributions from a Swiss Multicell Storm. *J. Appl. Meteor.*, **14**, 91–97.

Joss, J. and A. Waldvogel, 1967: Ein Spektograph fur Niederschlagstopfen mit Automatischer Auswertung, (A raindrop spectrograph with automatic analysis.) *Pure Appl. Geophys.* **68**, 240–246.

Lane, J. E., R. C. Youngquist, W. D. Haskell, and R. B. Cox, 2006: A hail size distribution impact transducer. JASA Express Letters, **119** (3), 57-53.

Lane, J., T. Kasparis, and, and L. Jones, 2002: A 3D drop-size distribution model based on the convolution of raindrops at terminal velocity. *International Journal of Remote Sensing*, **23** (15), 3115–3121.

Lane, J. E., T. Kasparis, L. Jones, and F. Merceret, 2002: Estimating a 3-D Drop Size Distribution and Examining Sensitivities to Vertical Air Motion. *NASA TRMM Science Conference*, Honolulu, HI.

Lane, J, T. Kasparis, and G. McFarquhar, 1997: Adaptive DSP algorithm for calibrating drop size distribution rain gauges, *SPIE AeroSense, 11th International Conference*, Orlando, FL.

Long, A.B., R.J. Matson, and E.L. Crow, 1980: The Hailpad: Materials, Data Reduction and Calibration. *J. Appl. Meteor.*, **19**, 1300–1313.

Lozowski, E.P., and G.S. Strong, 1978: On the Calibration of Hailpads. *J. Appl. Meteor.*, **17**, 521–528.

Marshall, J., and W.M. Palmer, 1948: The distribution of raindrops with size. *J. Atmos. Sci.*, **5**, 165–166.

McFarquhar, G.M., R. List, D.R. Hudak, R.P. Nissen, J. Dobbie, N. Tung, and T. Kang, 1996: Flux Measurements of Pulsating Rain with a Disdrometer and Doppler Radar during Phase II of the Joint Tropical Rain Experiment in Malaysia. *J. Appl. Meteor.*, **35**, 859–874.

Strong, G. S. and E. P. Lozowski,1977: An Alberta study to objectively measure hailfall intensity. *Atmos. Oceanic Phys*. **4**, 33–53.

Visser, P. J.M. and J. van Heerden, 2000: Comparisons of hail kinetic energy derived from radar reflectivity with crop damage reports over the eastern Free State. *Water SA*, **26** (1), 91-96.

Waldvogel, A., W. Schmid, and B. Federer, 1978: The Kinetic Energy of Hailfalls. Part I: Hailstone Spectra. *J. Appl. Meteor.*, **17**, 515–520.

Waldvogel, A., B. Federer, W. Schmid, and J.F. Mezeix, 1978: The Kinetic Energy of Hailfalls. Part II: Radar and Hailpads. *J. Appl. Meteor.*, **17**, 1680–1693.